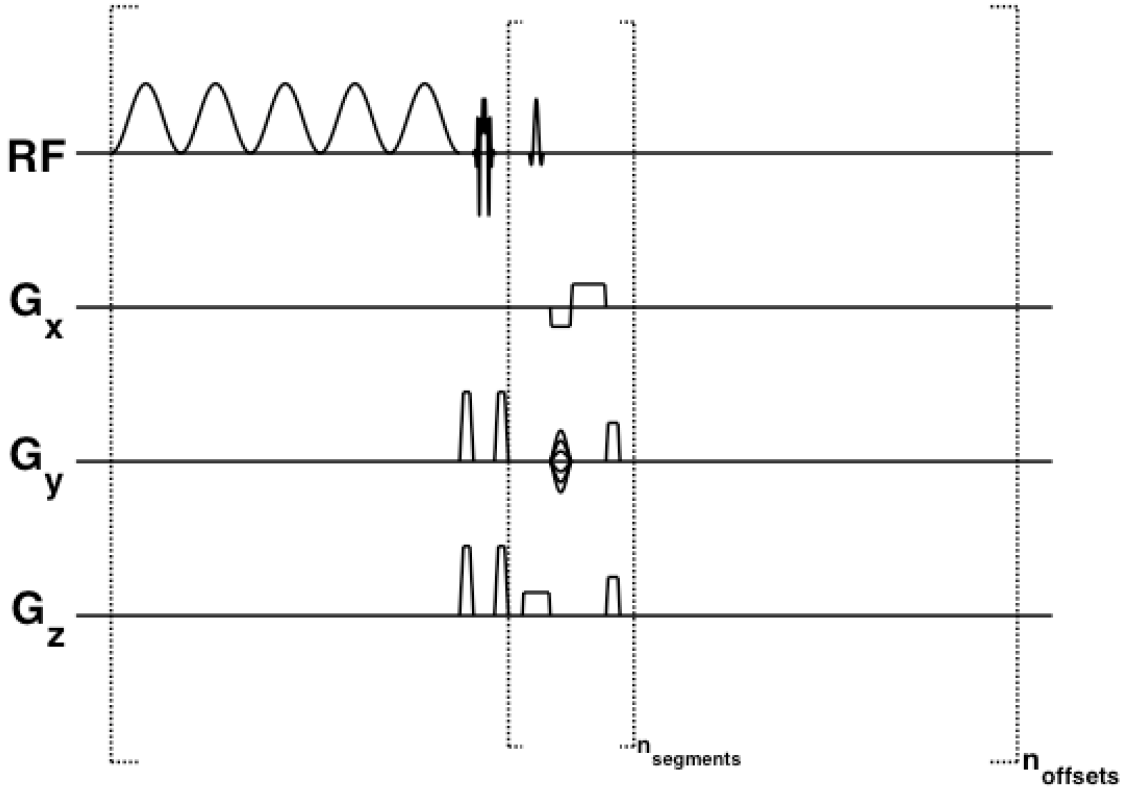

Supplementary Information Fig. S1. Pulse sequence diagram showing the implementation of CrCEST and WASSR sequences. The basic sequence structures are same for both CrCEST and WASSR, with only differences being range of offset frequency values being scanned, saturation powers being applied (2.9 μT for CrCEST vs. 0.29 μT for WASSR), and saturation duration (500 ms for CrCEST vs. 200 ms for WASSR).

The pulse sequence consisted of saturation pulse train followed by spoiler gradients. Following that, a chemical-shift-selective fat saturation pulse was applied to suppress the fat signal, followed by another set of spoiler gradients and then image readout using TurboFLASH readout was implemented.

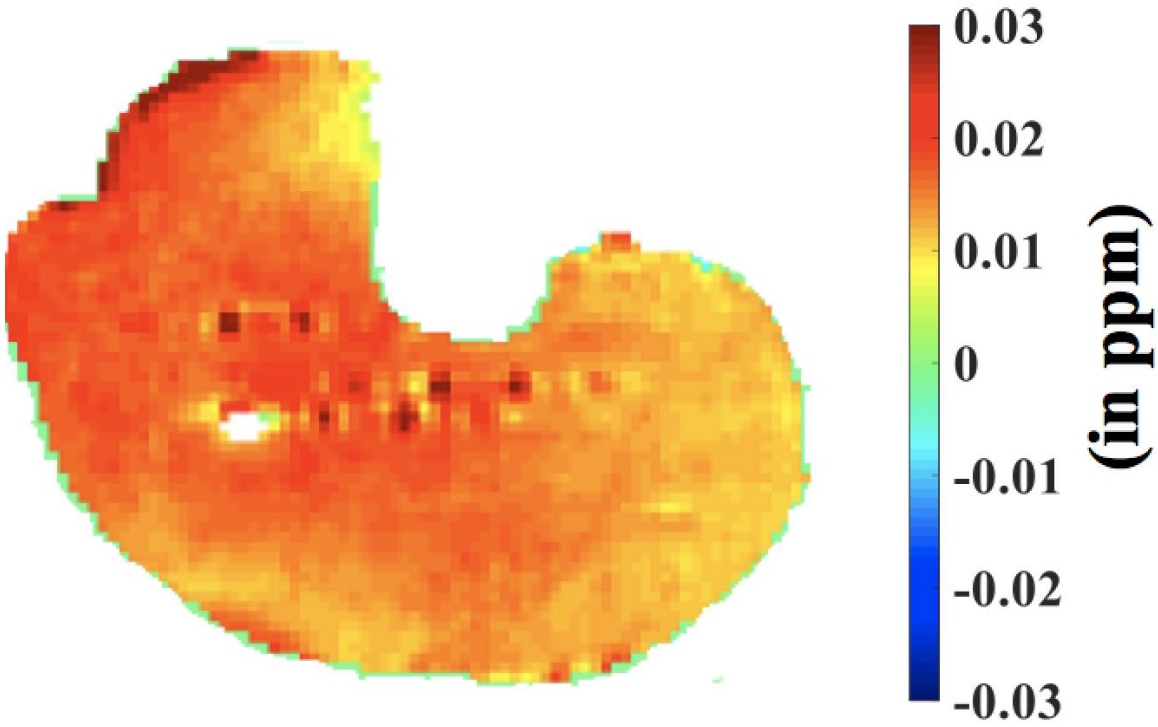

Supplementary Information Fig. S2. To assess the effect of the field drift, series of WASSR maps from the calf muscle at-rest were acquired for 10 minutes 40 seconds (temporal resolution = 70s; number of repetitions = 9; 2 dummy shots worth 10s). ΔB_0 map, calculated as the difference between 9^{th} (last) and 1^{st} WASSR maps, is shown here. B_0 shift was mostly less than 0.02 ppm (~6Hz). The center of frequency drift measured at the end of the scan, measured at the scanner, was ~6Hz.

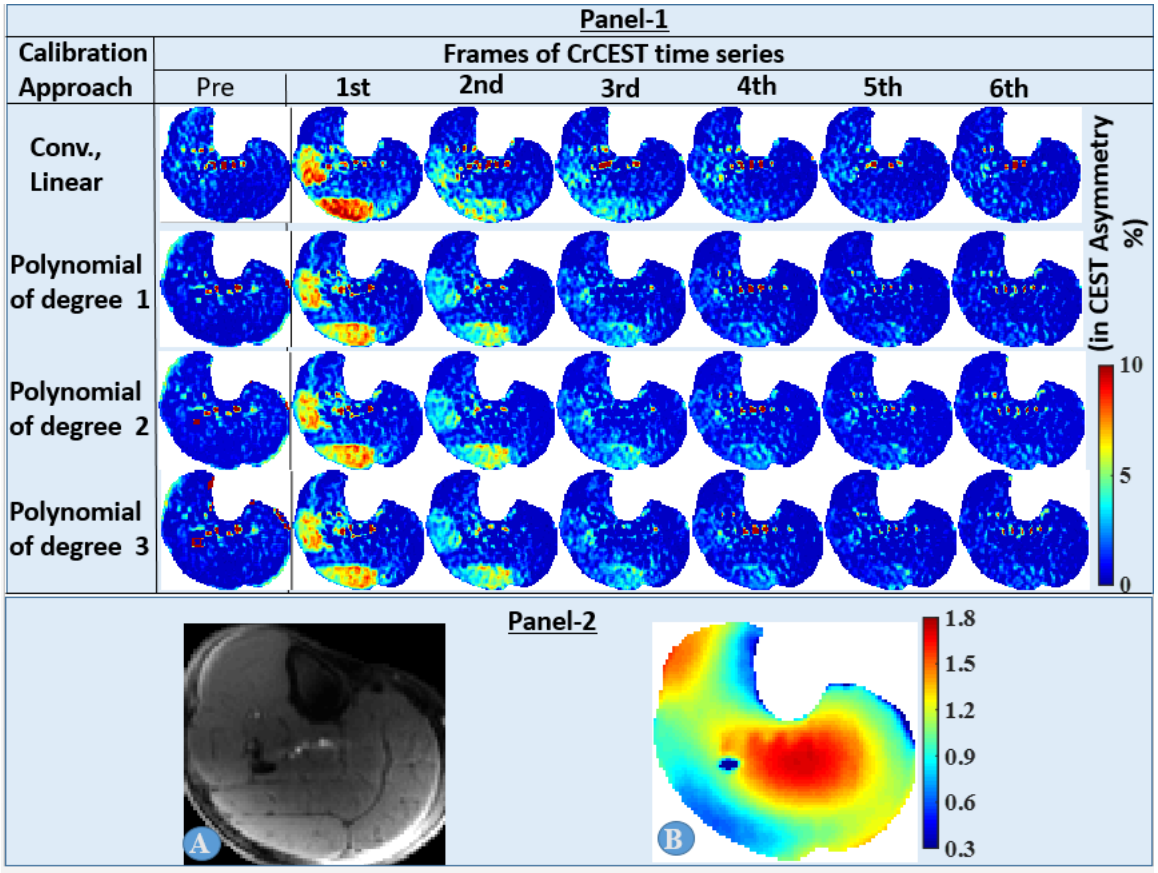

Supplementary Information Fig. S3: **Panel-1:** The effect of various B_1^+-calibration approaches on ΔCrCEST time-series is shown for the middle slice (5th out of 8 slices). **Panel-2:** Reference image (A) and B_1^+-map (B) for the same slice are also shown.

This figure contains information similar to Fig. 1, except ΔCrCEST time-series is shown here instead of CrCEST time-series as temporal trends are more conspicuous in former. Evidently, the conventional linear B_1^+-calibration approach led to higher post-exercise elevations and lower creatine decay constants. ΔCrCEST time-series showed similar temporal trends for all other three candidates, i.e. polynomials of degrees 1,2,3.

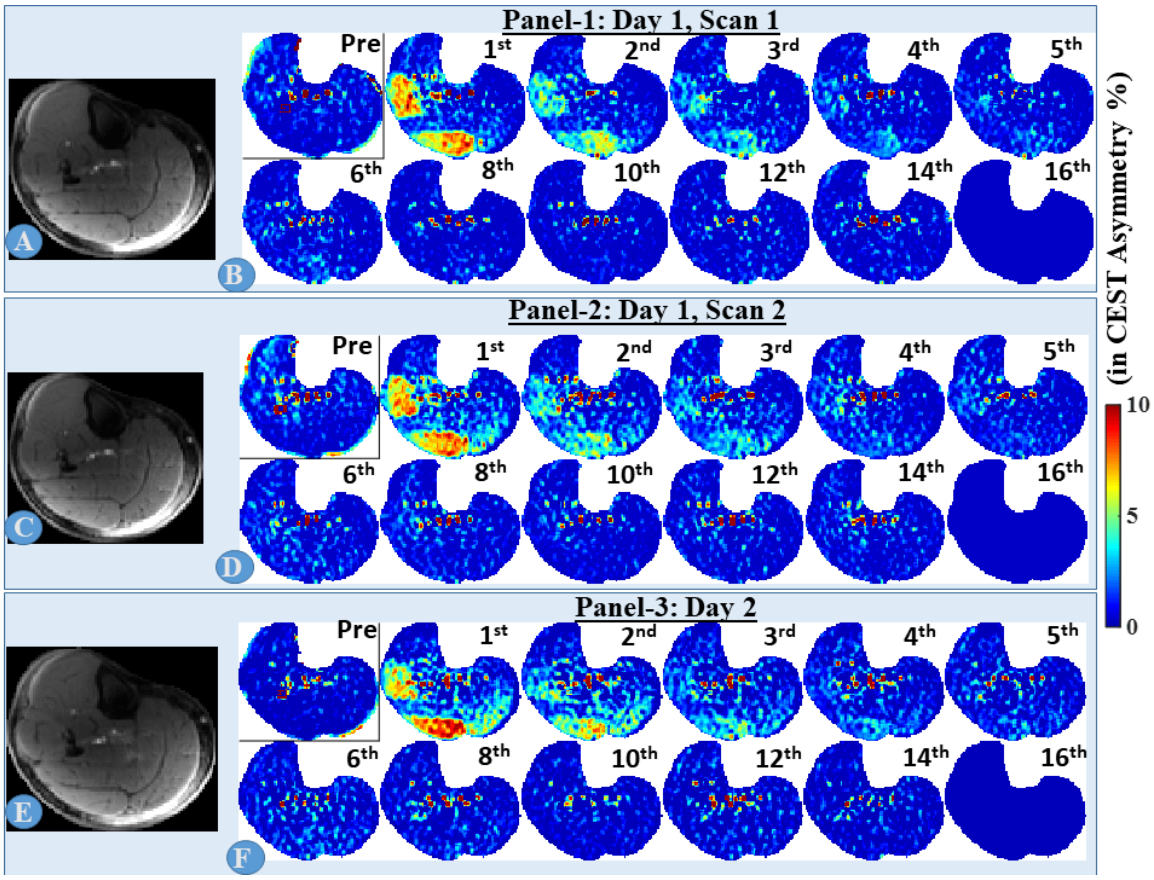

Supplementary Information Fig. S4: Inter- and intra-day ΔCrCEST time-series for volunteer #1, corresponding to the middle slice (5th out of 8 slices). A, C, D are matching anatomical (reference) slices for three inter-/intra-day scans and B, D and F are respective time-series for CrCEST maps. Only one out of four pre-exercise repetitions and selected time frames of post-exercise CrCEST time-series are being presented, with frame number written on right top corner of each frame. Both lateral gastrocnemius and peroneus longus were utilized during PFE.

This figure contains information similar to Fig. 3, except ΔCrCEST time-series is shown here instead of CrCEST time-series, as the temporal trends are more conspicuous in former.

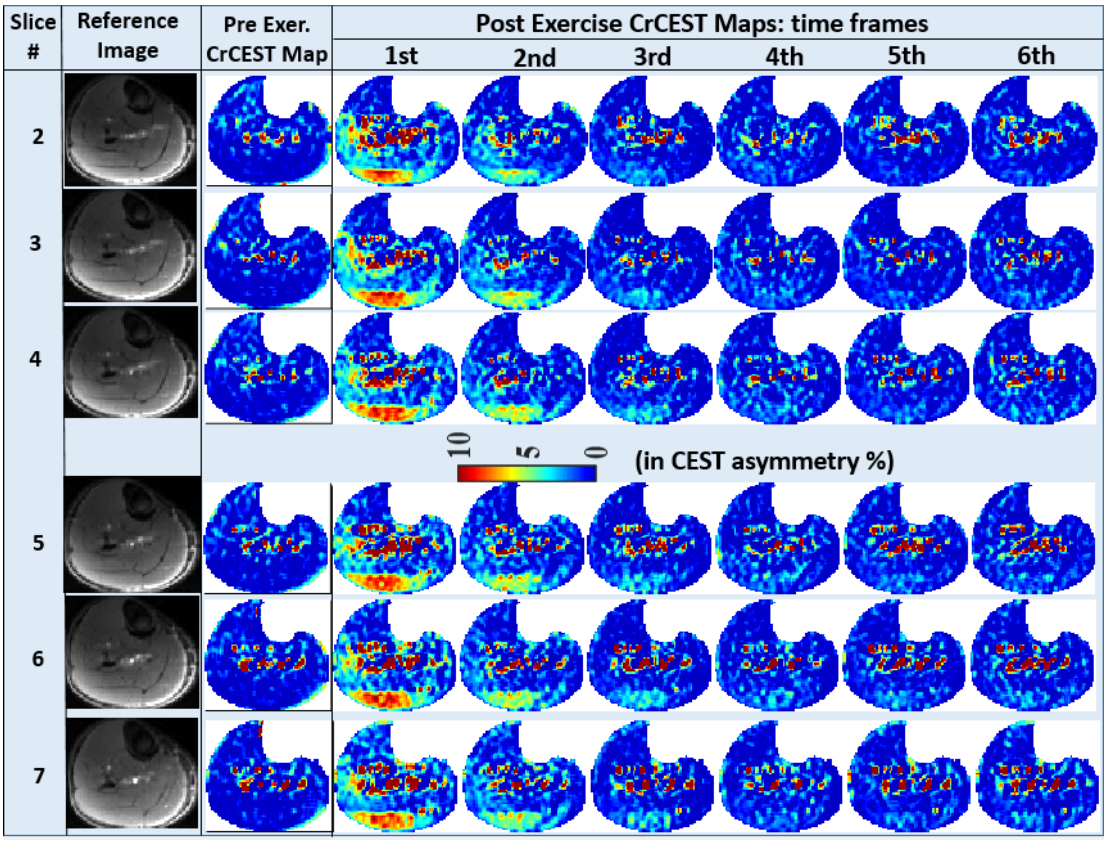

Supplementary Information Fig. S5: Time-series of ΔCrEST maps showing exercise-induced changes in skeletal muscle, using images from 2nd -7th slices of volunteer #5. Only one out of four pre-exercise CrCEST maps and selected time frames (first six out of sixteen) of post-exercise CrCEST maps are shown.

The temporal decay trends for LG and PL were similar across all slices (#2-7). The extent of participation of MG to PFE exercise load, as judged by post-exercise CrCEST elevation, varied across slices with earlier slices showing more involvement of LG.

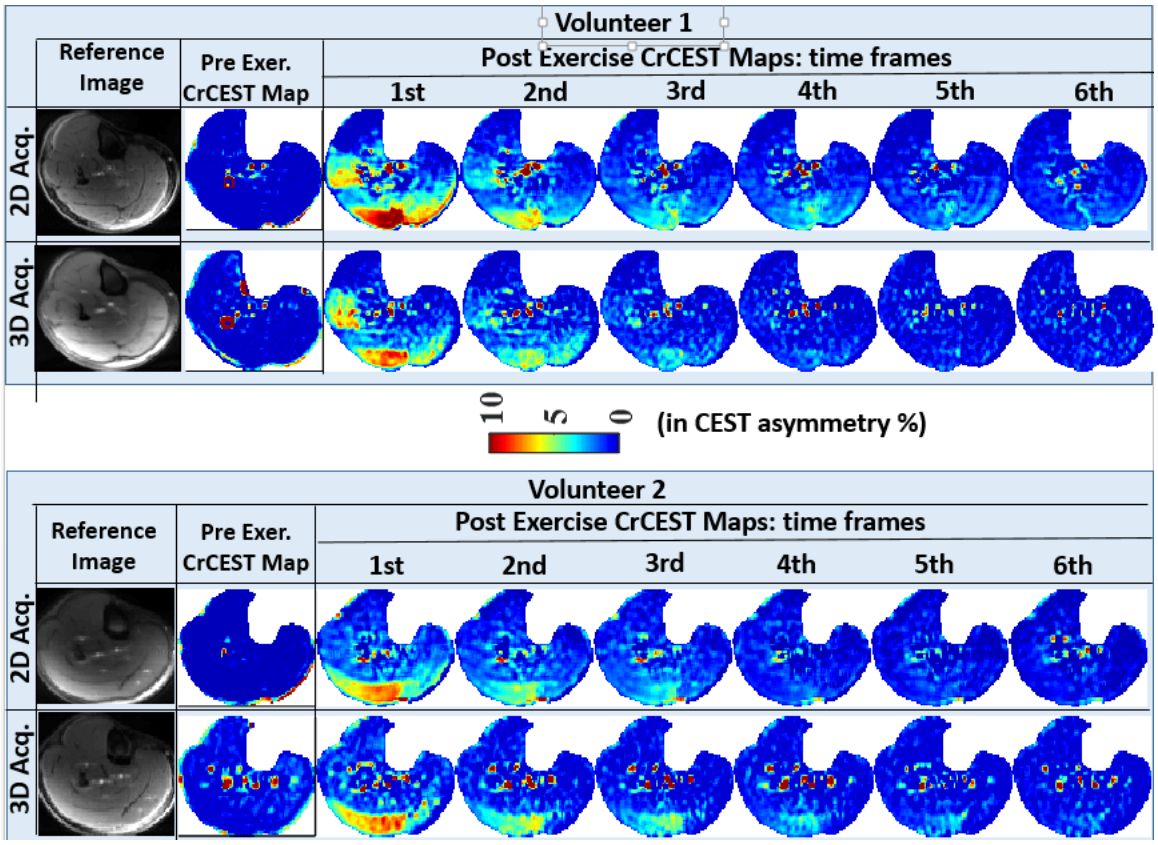

Supplementary Information Fig. S6: Time-series of ΔCrEST maps showing exercise-induced changes in skeletal muscle of two volunteers for both 2D and 3D acquisitions. Only one out of four pre-exercise CrCEST maps and selected time frames (first six out of sixteen) of post-exercise CrCEST maps are shown.

For a fair comparison, the thickness of 3D acquisition was increased to 10 mm (comparable to thickness of 2D comparison) for this analysis. On the other hand, parallel acquisition with tfl-FA of 5^{o} was used for 3D acquisition, whereas 2D acquisition involved tfl-FA of 10^{o} without parallel acquisition.

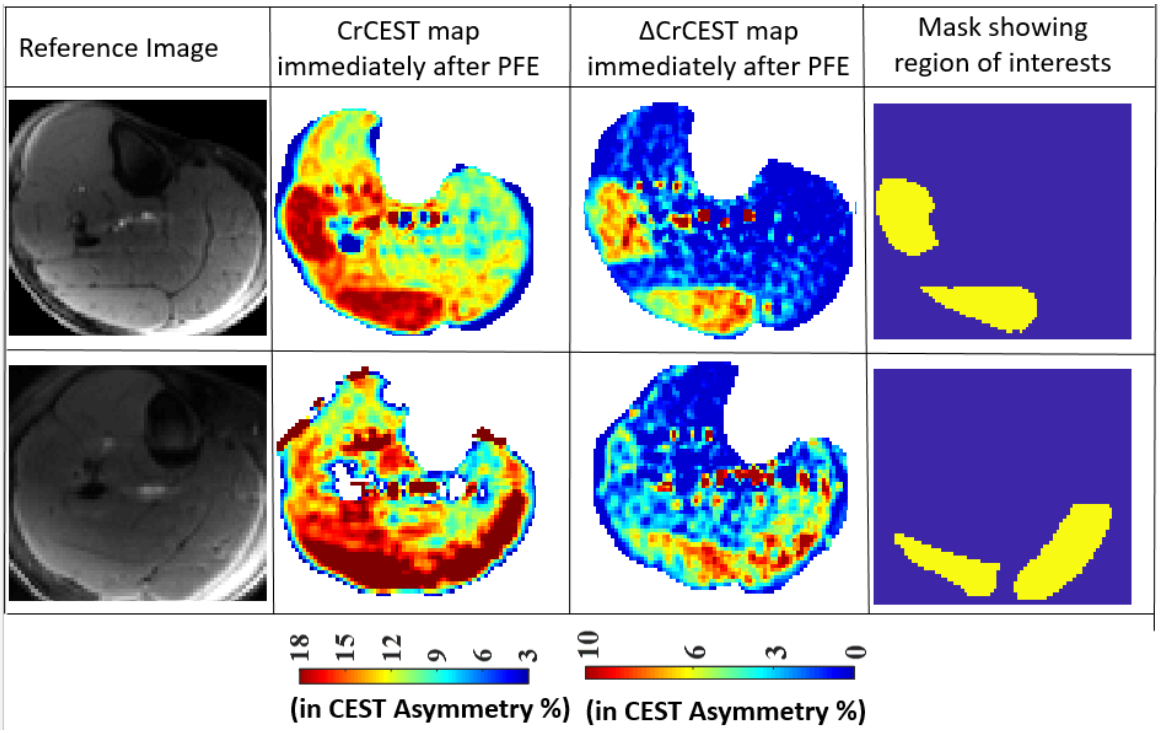

Supplementary Information Fig. S7: Typical muscle-group-specific masks chosen for two volunteers (#1, #4). Masks were constructed based on the reference image and CrCEST map/ ΔCrCEST map immediately post-exercise, as described in appendix D.

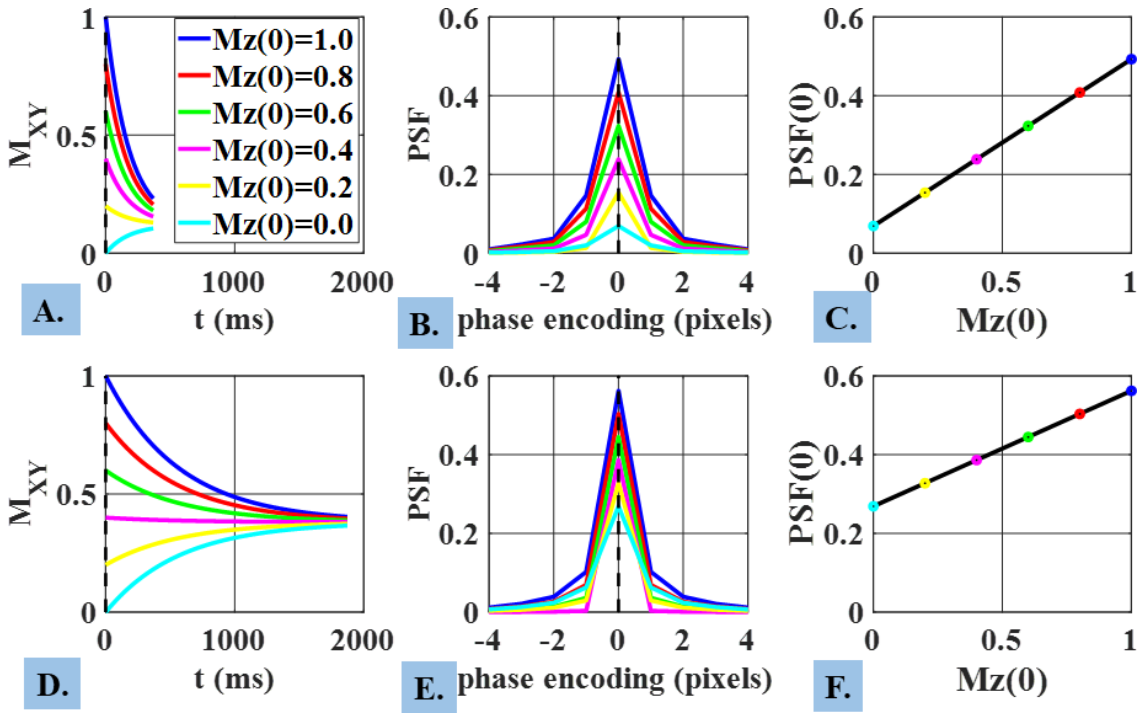

Supplementary Information Fig. S8: The evolution of transverse magnetization (M_{xy}) immediately after excitation/saturation pulses for 2D and 3D acquisitions are shown in (A) and (D). For longer readout duration, M_{xy} tends to reach to a steady state.

The point spread function (PSF) computed along the phase encoding direction for both the 2D and 3D GRE sequences with centric phase encoding order are displayed in (B) and (E). The blurring effects of these PSFs, typically characterized by the broadness of the peak at half the maximum magnitude, are all less than 2 pixels.

The correlation between $M_z(0)$ and PSF(0) for 2D and 3D acquisitions are plotted in (C) and (F). The linear correlations fit well for both type of acquisition. The 3D acquisition with longer readout reveal smaller slope, indicating declined resolving power due to longer readout.

Supplementary Information Tab. S1:

CrCEST asymmetry values for the activated muscle groups of volunteer 1, namely LG and PL, at rest and at the 1st time point of post-exercise acquired during day-1, session-1. LG and PL were the active muscle groups for this volunteer.

The reported standard deviation corresponds to voxel-wise CrCEST distribution across a particular muscle group with in the slice.

Slice No.	**CrCEST Asymmetry Values (%)**			
	LG		**PL**	
	At-rest	**1st time point of Post-exercise**	**At-rest**	**1st time point of Post-exercise**
2	11.98±1.86	17.98±2.17	12.13±2.41	16.04±5.25
3	12.22±1.94	18.44±1.99	11.70±2.28	16.03±5.03
4	12.18±2.03	18.67±2.18	12.14±2.52	16.24±4.99
5	12.11±1.88	18.56±2.46	12.40±2.36	16.40±5.18
6	11.78±1.96	18.33±2.45	12.98±2.38	16.98±5.38
7	11.75±1.98	18.32±2.36	13.53±2.54	17.10±5.83